Constraints on Axion Mediated Dipole-Dipole Interactions

Zitong Xu,[1] Xing Heng,[1] Guoqing Tian,[1] Di Gong,[2] Lei Cong,[3,4] Wei Ji,[5,3,4,*] Dmitry Budker,[3,6,7] and Kai Wei[1,2,8,†]

[1]School of Instrumentation Science and Opto-electronics Engineering, Beihang University, Beijing 100191, China
[2]Hangzhou Extremely Weak Magnetic Field Major Science and Technology Infrastructure Research Institute, Hangzhou 310051, China
[3]Johannes Gutenberg University, Mainz 55128, Germany
[4]Helmholtz Institute Mainz, Mainz 55128, Germany
[5]School of Physics and State Key Laboratory of Nuclear Physics and Technology, Peking University, Beijing 100871, China
[6]Helmholtz-Institute, GSI Helmholtzzentrum fur Schwerionenforschung, Mainz 55128, Germany
[7]Department of Physics, University of California at Berkeley, Berkeley, California 94720-7300, USA
[8]Hefei National Laboratory, Hefei 230088, China

(Received 7 December 2024; revised 22 February 2025; accepted 1 April 2025; published 6 May 2025)

The search for axions sits at the intersection of solving critical problems in fundamental physics, including the strong *CP* problem in QCD, uncovering the nature of dark matter, and understanding the origin of the Universe's matter-antimatter asymmetry. The measurement of axion mediated spin-dependent interactions offers a powerful approach for axion detection. However, it has long been restricted to regions outside the "axion window" due to a significant trade-off: the need to effectively suppress the magnetic leakage from highly polarized spin sources while simultaneously detecting subfemtotesla level exotic physics signals at sub-decimeter-scale distances. In this work, we report new experimental results on axion mediated exotic spin-spin interactions using an iron-shielded $SmCo_5$ spin source in combination with a specially designed self-compensation comagnetometer. Employing a composite shielding structure, we achieved a suppression of the magnetic field by up to 10^{11}. This enabled us to establish new constraints on the coupling between electrons and neutrons, improving previous experimental limits by up to 10 000 times within the axion window. Furthermore, we also set the strongest constraints on the coupling between electrons and protons. The proposed method holds substantial potential not only for advancing the search for new physics beyond the standard model but also for enabling transformative applications in biological and chemical research.

DOI: 10.1103/PhysRevLett.134.181801

The standard model of particle physics has been remarkably successful in explaining a wide range of phenomena but falls short in addressing several key issues, such as the nature of dark matter, dark energy, and matter-antimatter asymmetry in the Universe. These unresolved issues strongly suggest the existence of new physics beyond the standard model. To bridge these gaps, various theories beyond the standard model have proposed the existence of new light bosons [1,2], with particular focus on spin-0 axion and axionlike particles (ALPs) (in this Letter, we refer to both axions and ALPs as "axions") [3–5]. Axions are candidate constituents of cold dark matter. The challenge in the search for axions is that their mass is unknown and can, in principle, be of any value with a range spanning many orders of magnitude. Several theories constrain the most probable axion mass range to 0.01–1 meV [6–10], which is the so-called "axion window." However, previous laboratory haloscope experiments for axion dark matter research such as the Axion Dark Matter eXperiment (ADMX) [11] and astrophysical observations such as the SN1987A [12] and Sudbury Neutrino Observatory (SNO) [13] primarily explored mass ranges outside the window [5,14]. Recently, experimental efforts have shifted toward exploring the axion window, including haloscope experiments (Orpheus [15], MADMAX [16], ORGAN [17], and CAPP [18]).

If the axion exists, it could mediate exotic spin-dependent forces [19,20], which have garnered considerable attention in recent years [21,22]. Searches for spin-dependent forces have the advantage of covering a wide range of the axion mass without scanning. A comprehensive overview of theoretical and experimental developments is available in a recent review [22]. Numerous experimental approaches are used or have been proposed to investigate these forces, including torsional pendulums and oscillators [23], atomic

*Contact author: wei.ji@pku.edu.cn
†Contact author: weikai@buaa.edu.cn

magnetometers [24–28] and nitrogen-vacancy centers in diamond [29], nuclear magnetic resonance (NMR) [30,31], and other advanced technologies [32–34]. However, there are fewer experiments detecting it within the axion window [28,35]. The significant challenge is that measurements within the axion window demand that the distance between a sensitive detector and a high-spin-density source should be subdecimeter. Ideally, one could choose a high-spin-density source such as a $SmCo_5$ magnet and a high sensitivity atomic sensor to enhance the sensitivity to exotic interaction [22]. However, simultaneously achieving suppression of usual magnetic field leakage, which is about Earth's magnetic field, and ultrasensitive measurement of nonmagnetic exotic signal, which is subfemtotesla level in this range, is extremely challenging.

In this work, we tackle this challenge by employing a combination of advanced magnetic shielding and a self-compensation (SC) sensor. The SC sensor is designed to be insensitive to usual magnetic fields while retaining ultrahigh sensitivity to nonmagnetic fields. We report a method that achieves a magnetic field suppression factor of more than 10^{11} with the help of a composite magnetic shield consisting of three parts of structure to suppress the magnetic leakage of the spin source [36–38], as well as the suppression that comes from the use of a self-compensated magnetometer. Compared with the recent work to search for the axion in the axion window [28], the net spin in our spin source is more than 10^6-fold higher. Meanwhile, the sensitivity of our atomic sensor is also 2 orders of magnitude higher [39]. We apply this approach to search for exotic electron-neutron (or electron-proton) coupling in the range within the axion window. Having found no significant evidence for an axion mediated new force, we improve previous experimental constraints on electron-neutron coupling by up to 10 000 times, with typical improvements of 8000 times in the range of 0.02–0.1 meV, while the existing constraints [26] remain stronger below 0.009 meV. And we set the strongest constraints on electron-proton coupling. The approach demonstrated in this study exhibits significant potential for a wide range of biological and chemical applications that rely on the combination of a high-field prepolarization region and a low-field detection region.

Exotic dipole-dipole interactions—Among the various exotic interactions studied, specific terms take precedence based on the couplings under consideration, as detailed in Ref. [22]. In particular, the dipole-dipole term, which is the focus of this study, is significant because it provides the strongest constraints on the pseudoscalar-pseudoscalar couplings associated with axions [22]. The dipole-dipole interactions we measure in this experiment are

$$V_{pp} = -g_p^X g_p^Y \frac{\hbar^3}{16\pi c}\frac{1}{m_X m_Y}\left[\boldsymbol{\sigma}_X\cdot\boldsymbol{\sigma}'_Y\left(\frac{1}{r^3}+\frac{1}{\lambda r^2}+\frac{4\pi}{3}\delta(\boldsymbol{r})\right)\right.$$
$$\left.-(\boldsymbol{\sigma}_X\cdot\hat{\boldsymbol{r}})(\boldsymbol{\sigma}'_Y\cdot\hat{\boldsymbol{r}})\left(\frac{3}{r^3}+\frac{3}{\lambda r^2}+\frac{1}{\lambda^2 r}\right)\right]e^{-r/\lambda}, \quad (1)$$

where $\hbar$ is the reduced Planck constant, c is the speed of light, $\boldsymbol{\sigma}_X$ and $\boldsymbol{\sigma}'_Y$ are vectors of Pauli matrices representing the spins $\mathbf{s}_i = \hbar\boldsymbol{\sigma}_i/2$ of the two fermions X and Y, in our case, the electron and neutron/proton, m_X and m_Y are the corresponding masses, $\lambda = \hbar/m_a c$ is the force range, m_a is the axion mass, and r is the distance between two fermions. Here, we adopt the exotic potentials for macroscopic experiments as recommended in the review [22], and the $\delta(\mathbf{r})$ term is zero in our case, but is non-negligible on the atomic scale [40].

Experimental setup—The K-Rb-^{21}Ne comagnetometer in this experiment is similar to the one in Ref. [25]. There is a 12 mm diameter spherical cell containing 3.5 amagats of ^{21}Ne, 50 torr N_2, and K and Rb atoms with a density ratio of about $1/100$ at the center of the comagnetometer. The cell is heated to 190 °C. The K atoms are polarized with circularly polarized light tuned to the K-D1 line along the z axis. The Rb and ^{21}Ne atoms are spin polarized by spin exchange collisions. Hybrid optical pumping is utilized to improve the polarization uniformity. The precession of Rb atoms is detected with linearly polarized probe light propagating along the x axis.

The iron-shielded $SmCo_5$ (ISSC) spin source consists of a cylindrical $SmCo_5$ magnet with a diameter and height of 2.5 mm with remanence of about 1 T. The magnet is encased in a 2 mm thick layer of pure iron and a 2 mm thick layer of μ metal to minimize magnetic leakage. The core magnet and these shields together constitute what we define as the spin source. The primary advantage of the ISSC spin source is its combination of a low-leakage magnetic field with a large net spin, due to the differential contributions of orbital and spin moments to the total magnetization [41]. After adding the electron spins from both the $SmCo_5$ and the soft iron, the net number of spins is calculated to be 4.63×10^{20}. The direction of the source spin is modulated by rotating it with a servo motor around the z axis, during which the spin remains perpendicular to the z axis. An exotic pseudomagnetic field shown in Eq. (1) that interacts with the atomic spins in the comagnetometer would generate a potentially detectable sinusoidal signal.

These ISSC components are mounted on top of a long aluminum rod attached to a motor. The spin sensor is enclosed inside three layers of a μ-metal magnetic shield (μ cen). To minimize the interaction distance and magnetic noise of the shield, these three layers of shield are made of a tape-wound shield, centered on the cell location, with a radius of 40 mm. To further enhance shielding performance against magnetic leakage from the source in a confined space, a special small-volume shield (μ radial) is applied. Figure 1 illustrates the schematic of the composite shielding, while the detailed geometry and shield performance are presented in Fig. 2.

Magnetic field suppression—As shown in Fig. 1(a), the K-Rb-^{21}Ne comagnetometer is operated in the self-compensation regime to suppress the influence of real

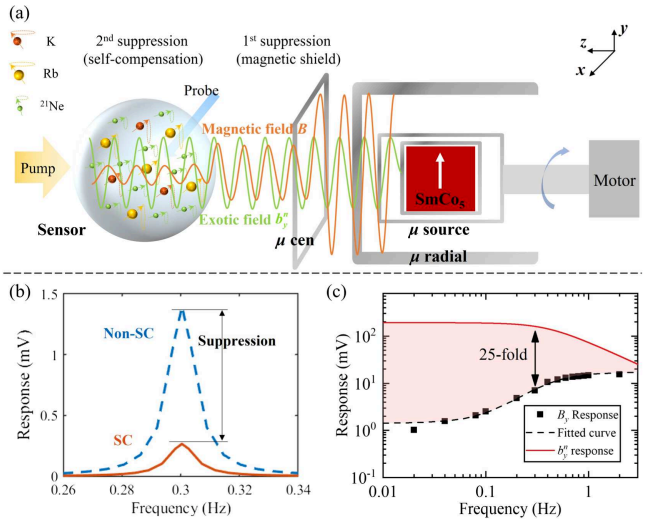

FIG. 1. Principle of the experiment. (a) The atomspins in the sensor cell are polarized and probed by pump and probe laser beams. The white arrow represents the magnetization direction of the spin source. A composite shield is used to shield the usual magnetic field from the spin source, named as first suppression, which contains the μ source for enclosing the spin source, the μ radial around the spin source, and the μ cen for enclosing the sensor. Besides, there are another two magnetic shields, one for enclosing the sensor and spin source, the other for enclosing the motor, which are not shown. The sensor works in the self-compensation (SC) regime to provide the second suppression of the magnetic field. Combining the first and second suppression, the magnetic field B (orange line) is significantly suppressed while the sensitivity to exotic field b_y^n (green line) is the highest. (b) The measured response to the magnetic field in the SC regime is significantly suppressed against that out of the SC. (c) In the SC regime, the comagnetometer is insensitive to the low-frequency magnetic field while the sensitivity of the exotic field is the highest. The response to the usual magnetic field is suppressed by 25 times at 0.3 Hz compared with the exotic field under the same condition. The measured frequency response is fitted with Bloch equations.

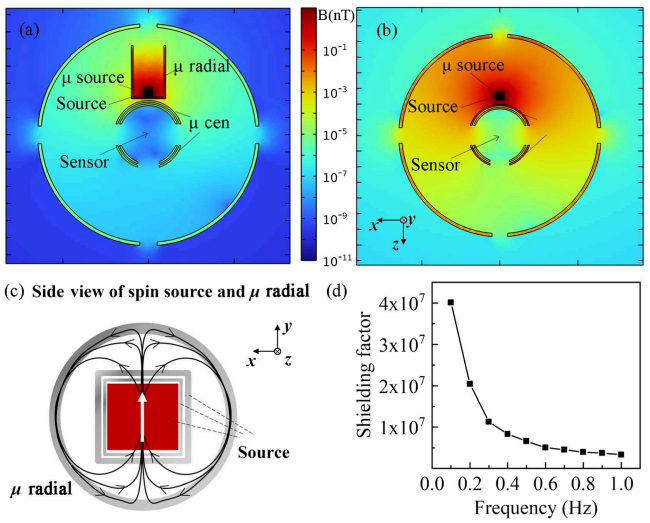

FIG. 2. Magnetic shield structure and performance. The magnetic shield structure (a) with the μ-radial shield has much better performance than the structure (b) without the μ-radial shield. μ source, shields of the spin source; μ radial, radial shield; μ cen, central tape-wound shield. (c) The μ radial is designed to be placed to form a closed magnetic loop between the μ radial and the spin source. (d) The measured shielding factor of the μ cen, μ radial, and self-compensation property together is over 1×10^7 at the target frequency.

magnetic fields. At the same time, the Fermi-contact interaction between ^{21}Ne nuclei and alkali electrons increases the signal generated by the exotic field [39,42,43]. According to the Bloch equations [25,42] describing the coupled spin ensembles, the comagnetometer's response to the quasistatic signal in the self-compensation regime is

$$P_x^e = \frac{P_z^e \gamma^e R_2^e}{R_2^{e2} + \gamma^{e2} \delta B_z{}^2} \left\{ b_y^n - b_y^e + \frac{\delta B_z}{B_z^n} B_y \right\}, \qquad (2)$$

where γ^e is the gyromagnetic ratio of the electron; P_z^e and R_2^e are the electron spin polarization and its transverse relaxation rate; b_y^n and b_y^e are the exotic fields along the y axis that couple with nuclei and electrons. $\delta B_z = B_z - B_c$ is the difference between the bias field B_z and the self-compensation point B_c. $B_c = -B_z^n - B_z^e$ is equal in magnitude but opposite in direction to the sum of the nuclear spin effective magnetic field B_z^n and the electronic spin effective magnetic field B_z^e. The spin polarization P_x^e is transformed to the output electric signal with a gain factor. When $\delta B_z = 0$, the comagnetometer works in the SC regime, where the response to usual magnetic fields B_y is near zero. The mechanism behind the SC regime is that the magnetization of noble-gas nuclear spins adiabatically follows the total magnetic field while its magnetization compensates B_y [39,44]. We demonstrate the SC regime by comparing the measured responses to B_y in and out of the SC regime by changing the bias field, as shown in Fig. 1(b). The response to B_y is significantly suppressed in the SC regime.

We use the same method as Refs. [39,43] to simulate the response to the exotic field b_y^n with the measured responses to the usual magnetic field B_y based on the coupled Bloch equations. The responses to b_y^n and B_y are illustrated in Fig. 1(c). The SC regime works with frequencies below 1 Hz, where the response to the usual magnetic field is greatly suppressed compared with the response above 1 Hz. Meanwhile, the response to the exotic field is the highest in the SC regime, which is significantly higher than that of B_y. The suppression factor can be more than 10^4 when the real magnetic field is dc. To optimize the sensitivity to the spin-spin interaction, the spin source is rotated at the frequency where the response to the exotic field b_y^n is high. Meanwhile, to avoid the effect of the large residual usual

magnetic field and the $1/f$ noise in low frequencies, we need to modulate the source at a relatively higher frequency within the SC regime. Our compromise is to modulate the exotic field at 0.3 Hz, where the response to B_y is suppressed by 25 times more than the response of b_y^n.

The top view of the entire shielding structure is presented in Figs. 2(a) and 2(b), showing simulations of the magnetic shielding effectiveness with and without the blue μ-radial shield, respectively. The direction of magnetization of the spin source is perpendicular to the axial direction of the μ radial. Thus, a closed magnetic loop is formed by the side wall as shown in Fig. 2(c). The inclusion of the μ-radial shield enhances the shielding performance by more than 100 times within a limited space compared to the structure without the μ-radial shield.

The integrated magnetic suppression performance of the shield structure and the self-compensation ability is tested with an electromagnet with similar dimensions as the source, and its amplitude and frequency are tuned by changing the current through it. The leakage of the magnetic field can be estimated as $B^l_{\rm cell}(f) = B^l_{\rm ori}/\chi(f)$, where $B^l_{\rm ori}$ is the leakage of the source, which is measured to be approximately 1 nT at a distance of 2 cm, $\chi(f)$ is the decay factor of the magnetic leakage, which includes the geometrical decay factor (of the residual distance), the shielding factor of μ-radial and μ-cen shielding, and the suppression factor of the SC mode. Figure 2(d) shows the measured shielding factor of $\chi(f)$. At the working frequency of 0.3 Hz, we calibrate the $\chi(0.3\ \text{Hz}) > 1 \times 10^7$, and the magnetic leakage at the position of the sensor is estimated to be smaller than 0.1 fT. We can also consider the traditional definition of the shielding factor comparing the situations with and without the shielding. The magnetic leakage is estimated to be 10 μT at the position of the sensor, which means that our magnetic shielding factor together with the SC mode is about 10^{11}.

Result—The signal of the comagnetometer and the pulse signal from the motor decoder, used for signal synchronization, are simultaneously acquired by a data acquisition device. The modulated exotic field applied on the sensor spins can be considered as an equivalent magnetic field by integrating the overall contributions from the spins in the source with $b^{n,p} = \eta^{n,p}/\mu_N \int V_{pp} dV$, where $\eta^n = 0.58$ and $\eta^p = 0.04$ are the fraction factors for neutron and proton spin polarization, while μ_N is the magnetic moment of the ^{21}Ne nucleus. The detailed data processing procedure and the evaluation of the phase uncertainty, as summarized in Table I, are provided in the End Matter. The exotic field b_y^n is derived from sensor signal S by $S = K_{b_y^n} b_y^n$. The calibration factor $K_{b_y^n}$ of b_y^n is determined by the measured response to the usual magnetic field [25,42,45]. Moreover, we consider the difference between the dc and ac response factors with a ratio $K^{\rm ac}_{b_y^n}/K^{\rm dc}_{b_y^n}$ as shown in Fig. 4(e) in the End Matter. For 0.3 Hz, $K^{\rm ac}_{b_y^n}$ is determined to be 0.84(6).

TABLE I. The experimental parameters and their error budget for the coupling coefficients.

Parameter	Value	$\Delta g_p^e g_p^n (\times 10^{-10})$[a]
Net spin ($\times 10^{20}$)	4.63(56)	-0.41
		$+0.51$
Mounting error (deg)	± 2.00	± 0.18
r (mm)	50.00(5)	± 0.04
Phase uncertainty (deg)	± 1.57	± 0.15
$K^{\rm AC}_{b_y^n}$ (μV/fT)	1.09(10)	-0.32
		$+0.38$
Magnetic leakage (fT)	< 0.10	< 4.75
Total		$\pm 10.8_{\rm stat} \pm 4.8_{\rm syst}$[b]

[a]The contribution to the error budget at $\lambda = 7$ mm.
[b]Error contribution from the uncertainties listed above.

Using all the 80 h data, the exotic field b_y^n is measured to be $(0.08 \pm 0.22_{\rm stat} \pm 0.12_{\rm syst})$ fT as shown in Fig. 3(a). The systematic error mainly comes from magnetic leakage and the uncertainty of the calibration factor $K^{\rm ac}_{b_y^n}$. As shown in Table I, other systematic uncertainties that arise from the experimental setup and physics simulations, including position uncertainties, the phase uncertainty of the comagnetometer, the net spin simulation errors, and the mounting error (misalignment) of the spin source, are also accounted in analysis of the uncertainty of the coupling constant. At a force range of 7 mm (equivalent to an axion mass of about 0.03 meV), since no significant evidence for the axion mediated force is found, taking into account various systematic uncertainties as well as the statistical uncertainty, new limits on the dimensionless coupling factor of the new force are obtained. The coupling constant is determined to be $g_p^e g_p^n = (0.38 \pm 1.08_{\rm stat} \pm 0.48_{\rm syst}) \times 10^{-9}$, and we set a limit $|g_p^e g_p^n| \leqslant 2.4 \times 10^{-9}$ with a 95% confidence level, improving on the previous limit [28] at 0.03 meV by over 4 orders of magnitude. The limit for other force ranges is determined with the same method, as shown in Fig. 3(b). Furthermore, taking the contribution of the proton spin in the ^{21}Ne nucleus into account, we establish the strongest constraints on the coupling between electrons and protons, as shown in Fig. 3(c). There is no reported electron-proton coupling in this range, and we include the electron antiproton coupling from antiprotonic helium result as a comparison [46]. Constraints between electron and proton interactions also exist at shorter force ranges [40,47]. A NMR resonance enhancement experiment is also proposed to detect axions within this force range [48].

The long-term stability of the comagnetometer was monitored over a period of more than 24 h, revealing that the fluctuation of the key parameter, the self-compensation point, was less than 0.3% of its mean value. However, drift in the self-compensation point introduces errors in the calibration factor $K^{\rm ac}_{b_y^n}$. These uncertainties are summarized in Table I. The long-term stability is because of many

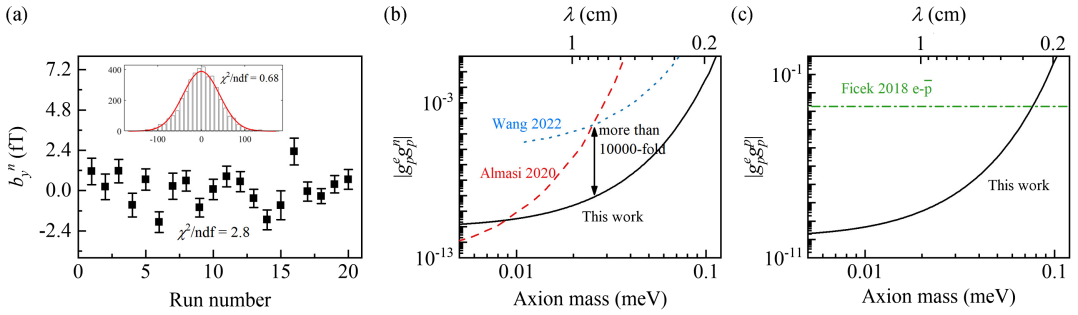

FIG. 3. Experimental results. (a) Each point represents an average of a 4 h measurement. The error bars represent the statistical and systematic error of the comagnetometer. The exotic field b_y^n is measured to be $(0.08 \pm 0.22_{\mathrm{stat}})$ fT. Inset: histogram of a 4 h dataset with a Gaussian fit in the red line. (b) The experimental limits on $|g_p^e g_p^n|$. The blue dotted line, "Wang 2022," is from Ref. [28]; the red dashed line, "Almasi 2020," is from Ref. [26]. Almasi 2020 is more sensitive at low axion masses due to a larger spin source. The main gain over Wang 2022 is the use of a higher-density (solid) spin source and a higher-sensitivity sensor in this work. (c) The experimental limits on $|g_p^e g_p^p|$. The green dash-dotted line, "Ficek 2018 e-p̄," is from Ref. [46].

technical improvements [25] such as a vibration isolation system to mitigate vibration noise [49], a closed-loop temperature control system to stabilize spin polarization and calibration factors, a vacuum system to reduce thermal convection, optical noise suppression techniques [50], and the method to enhance the SC stability [39].

Future improvements will focus on detecting exotic forces at shorter ranges with higher sensitivity. The primary challenge remains the trade-off between reducing magnetic leakage and increasing the density of the spin source. In this work, we addressed this issue by designing a specially structured shield to create a magnetic loop, enhancing shielding performance by 100-fold within a compact volume. Further advancements require shields made of materials with higher permeability and lower noise to achieve better suppression of magnetic leakage and further improve sensitivity.

Furthermore, our approach offers broader possibilities for applications requiring both high magnetic field regions and ultralow magnetic field regions. As a case study, we focus on the zero- to ultralow-field nuclear magnetic resonance (ZULF-NMR) technique in biological and chemical research [51,52]. ZULF-NMR necessitates spatially distinct areas: a tesla level magnetic field region for prepolarization and an ultralow magnetic field region (at the femtotesla level) for NMR signal detection. Conventional setups employ cylindrical magnetic shielding and maintain a significant gap (approximately 40 cm) between the high- and low-field regions, introducing notable signal attenuation due to relaxation effects [51,53–55]. However, the compact shielding structure presented here reduces the sample transportation time by up to an order of magnitude and reduces the setup volume by over 15-fold. For ZULF-NMR experiments, the shielding factor of the μ source and μ radial is improved to 10^8, even with a 6 mm diameter axial hole for sample shuttling. The reduction in distance and time enabled by our design provides significant advantages in preserving signal integrity and simplifying the experimental setup.

Conclusion—In conclusion, we utilized a comagnetometer and a specially designed spin source to search for exotic dipole-dipole interaction. The usual magnetic field from the source is suppressed by over 11 orders of magnitude, due to source and sensor shielding and the use of the self-compensation regime, while maintaining the ultrahigh sensitivity to the exotic field. With the high spin density of the source, we have improved the limit on the spin-dependent interaction between electrons and neutrons within the axion window, achieving a remarkable improvement of over 10 000 times at 0.03 meV. We also set the strongest constraints on the coupling between electrons and protons, which previously have only been reported through analysis of spectroscopy data from antiprotonic helium [46]. In future work, the experimental methods developed here will be applied to a broader search for exotic spin-dependent interactions, search for dark matter directly coupled to atomic spins, and study of spin-gravity interaction. New limits can be set on coupling parameters for spin-1 bosons [22], such as the Z' boson, and also for the study of violations of parity symmetry, as discussed in Ref. [56].

Acknowledgments—K. W. was funded by the National Science Foundation of China (NSFC) under Grants No. 62203030 and No. 61925301 for Distinguished Young Scholars, by the Innovation Program for Quantum Science and Technology under Grant No. 2021ZD0300401, and by the Fundamental Research Funds for the Central Universities. W. J. and D. B. were funded by the DFG Project ID 390831469: EXC 2118 (PRISMA+Cluster of Excellence), by the COST Action within the project COSMIC WISPers (Grant No. CA21106), and by the QuantERA project LEMAQUME (DFG Project No. 500314265).

[1] R. D. Peccei and H. R. Quinn, Constraints imposed by *CP* conservation in the presence of instantons, Phys. Rev. D **16**, 1791 (1977).

[2] P. W. Graham, D. E. Kaplan, J. Mardon, S. Rajendran, W. A. Terrano, L. Trahms, and T. Wilkason, Spin precession experiments for light axionic dark matter, Phys. Rev. D **97**, 055006 (2018).

[3] P. Athron, C. Balázs, A. Beniwal, J. E. Camargo-Molina, A. Fowlie, T. E. Gonzalo, S. Hoof, F. Kahlhoefer, D. J. Marsh, M. T. Prim *et al.*, Global fits of axion-like particles to XENON1T and astrophysical data, J. High Energy Phys. 05 (2021) 159.

[4] R. T. Co, L. J. Hall, and K. Harigaya, Predictions for axion couplings from ALP cogenesis, J. High Energy Phys. 01 (2021) 172.

[5] I. M. Bloch, Y. Hochberg, E. Kuflik, and T. Volansky, Axion-like relics: New constraints from old comagnetometer data, J. High Energy Phys. 01 (2020) 167.

[6] M. S. Turner, Windows on the axion, Phys. Rep. **197**, 67 (1990).

[7] A. Youdin, D. Krause Jr, K. Jagannathan, L. Hunter, and S. Lamoreaux, Limits on spin-mass couplings within the axion window, Phys. Rev. Lett. **77**, 2170 (1996).

[8] S. Borsányi, Z. Fodor, J. Guenther, K.-H. Kampert, S. Katz, T. Kawanai, T. Kovacs, S. Mages, A. Pasztor, F. Pittler *et al.*, Calculation of the axion mass based on high-temperature lattice quantum chromodynamics, Nature (London) **539**, 69 (2016).

[9] V. B. Klaer and G. D. Moore, The dark-matter axion mass, J. Cosmol. Astropart. Phys. 11 (2017) 049.

[10] G. Ballesteros, J. Redondo, A. Ringwald, and C. Tamarit, Unifying inflation with the axion, dark matter, baryogenesis, and the seesaw mechanism, Phys. Rev. Lett. **118**, 071802 (2017).

[11] N. Du *et al.* (ADMX Collaboration), Search for invisible axion dark matter with the axion dark matter experiment, Phys. Rev. Lett. **120**, 151301 (2018).

[12] J. Engel, D. Seckel, and A. C. Hayes, Emission and detectability of hadronic axions from SN1987A, Phys. Rev. Lett. **65**, 960 (1990).

[13] A. Bhusal, N. Houston, and T. Li, Searching for solar axions using data from the Sudbury Neutrino Observatory, Phys. Rev. Lett. **126**, 091601 (2021).

[14] T. Wu, J. W. Blanchard, G. P. Centers, N. L. Figueroa, A. Garcon, P. W. Graham, D. F. J. Kimball, S. Rajendran, Y. V. Stadnik, A. O. Sushkov, A. Wickenbrock, and D. Budker, Search for axionlike dark matter with a liquid-state nuclear spin comagnetometer, Phys. Rev. Lett. **122**, 191302 (2019).

[15] G. Rybka, A. Wagner, K. Patel, R. Percival, K. Ramos, and A. Brill, Search for dark matter axions with the Orpheus experiment, Phys. Rev. D **91**, 011701(R) (2015).

[16] P. Brun, A. Caldwell, L. Chevalier, G. Dvali, P. Freire, E. Garutti, S. Heyminck, J. Jochum, S. Knirck, M. Kramer *et al.*, A new experimental approach to probe QCD axion dark matter in the mass range above 40 μeV, Eur. Phys. J. C **79**, 1 (2019).

[17] A. Quiskamp, B. T. McAllister, P. Altin, E. N. Ivanov, M. Goryachev, and M. E. Tobar, Direct search for dark matter axions excluding ALP cogenesis in the 63- to 67-μeV range with the ORGAN experiment, Sci. Adv. **8**, eabq3765 (2022).

[18] Y. Kim, J. Jeong, S. Youn, S. Bae, K. Lee, A. F. van Loo, Y. Nakamura, S. Oh, T. Seong, S. Uchaikin, J. E. Kim, and Y. K. Semertzidis, Experimental search for invisible dark matter axions around 22 μeV, Phys. Rev. Lett. **133**, 051802 (2024).

[19] J. Moody and F. Wilczek, New macroscopic forces?, Phys. Rev. D **30**, 130 (1984).

[20] B. A. Dobrescu and I. Mocioiu, Spin-dependent macroscopic forces from new particle exchange, J. High Energy Phys. 11 (2006) 005.

[21] M. Safronova, D. Budker, D. DeMille, D. F. J. Kimball, A. Derevianko, and C. W. Clark, Search for new physics with atoms and molecules, Rev. Mod. Phys. **90**, 025008 (2018).

[22] L. Cong, W. Ji, P. Fadeev, F. Ficek, M. Jiang, V. V. Flambaum, H. Guan, D. F. J. Kimball, M. G. Kozlov, Y. V. Stadnik *et al.*, Spin-dependent exotic interactions, Rev. Mod. Phys., https://journals.aps.org/rmp/accepted/ce070E03Pf11a308e1b040116e287416ae8a6ded6 (2025).

[23] S. Aldaihan, D. E. Krause, J. C. Long, and W. M. Snow, Calculations of the dominant long-range, spin-independent contributions to the interaction energy between two nonrelativistic Dirac fermions from double-boson exchange of spin-0 and spin-1 bosons with spin-dependent couplings, Phys. Rev. D **95**, 096005 (2017).

[24] W. Ji, W. Li, P. Fadeev, F. Ficek, J. Qin, K. Wei, Y.-C. Liu, and D. Budker, Constraints on spin-spin velocity-dependent interactions, Phys. Rev. Lett. **130**, 133202 (2023).

[25] K. Wei, W. Ji, C. Fu, A. Wickenbrock, V. V. Flambaum, J. Fang, and D. Budker, Constraints on exotic spin-velocity-dependent interactions, Nat. Commun. **13**, 7387 (2022).

[26] A. Almasi, J. Lee, H. Winarto, M. Smiciklas, and M. V. Romalis, New limits on anomalous spin-spin interactions, Phys. Rev. Lett. **125**, 201802 (2020).

[27] Y. J. Kim, P.-H. Chu, and I. Savukov, Experimental constraint on an exotic spin-and velocity-dependent interaction in the sub-meV range of axion mass with a spin-exchange relaxation-free magnetometer, Phys. Rev. Lett. **121**, 091802 (2018).

[28] Y. Wang, H. Su, M. Jiang, Y. Huang, Y. Qin, C. Guo, Z. Wang, D. Hu, W. Ji, P. Fadeev *et al.*, Limits on axions and axionlike particles within the axion window using a spin-based amplifier, Phys. Rev. Lett. **129**, 051801 (2022).

[29] M. Jiao, M. Guo, X. Rong, Y.-F. Cai, and J. Du, Experimental constraint on an exotic parity-odd spin-and velocity-dependent interaction with a single electron spin quantum sensor, Phys. Rev. Lett. **127**, 010501 (2021).

[30] H. Su, Y. Wang, M. Jiang, W. Ji, P. Fadeev, D. Hu, X. Peng, and D. Budker, Search for exotic spin-dependent interactions with a spin-based amplifier, Sci. Adv. **7**, eabi9535 (2021).

[31] Z. Xu, X. Ma, K. Wei, Y. He, X. Heng, X. Huang, T. Ai, J. Liao, W. Ji, J. Liu *et al.*, Constraining ultralight dark matter through an accelerated resonant search, Commun. Phys. **7**, 226 (2024).

[32] H. Yan and W. M. Snow, New limit on possible long-range parity-odd interactions of the neutron from neutron-spin rotation in liquid ^{4}He, Phys. Rev. Lett. **110**, 082003 (2013).

[33] Y. V. Stadnik, V. A. Dzuba, and V. V. Flambaum, Improved limits on axionlike-particle-mediated P, T-violating interactions between electrons and nucleons from electric dipole

moments of atoms and molecules, Phys. Rev. Lett. **120**, 013202 (2018).
[34] X. Ren, J. Wang, R. Luo, L. Yin, J. Ding, G. Zeng, and P. Luo, Search for an exotic parity-odd spin-and velocity-dependent interaction using a magnetic force microscope, Phys. Rev. D **104**, 032008 (2021).
[35] H. Su, M. Jiang, Y. Wang, Y. Huang, X. Kang, W. Ji, X. Peng, and D. Budker, New constraints on axion-mediated spin interactions using magnetic amplification, Phys. Rev. Lett. **133**, 191801 (2024).
[36] T. Sumner, J. Pendlebury, and K. Smith, Convectional magnetic shielding, J. Phys. D **20**, 1095 (1987).
[37] X. Xu, W. Liu, Y. Huang, W. Li, and S. Che, Magnetic shielding mechanism and structure design of composites at low frequency: A review, J. Magn. Magn. Mater. **570**, 170509 (2023).
[38] L. Yuan, P. Cui, H. Zhang, F. Zhao, Y. Li, L. Zhang, Y. Zheng, and Z. Yang, Comprehensive analysis and structural optimization for single-ended open magnetic shielding cylinder, IEEE Sens. J. **25**, 625 (2024).
[39] K. Wei, T. Zhao, X. Fang, Z. Xu, C. Liu, Q. Cao, A. Wickenbrock, Y. Hu, W. Ji, J. Fang *et al.*, Ultrasensitive atomic comagnetometer with enhanced nuclear spin coherence, Phys. Rev. Lett. **130**, 063201 (2023).
[40] P. Fadeev, F. Ficek, M. G. Kozlov, D. Budker, and V. V. Flambaum, Pseudovector and pseudoscalar spin-dependent interactions in atoms, Phys. Rev. A **105**, 022812 (2022).
[41] W. Ji, C. B. Fu, and H. Gao, Searching for new spin-dependent interactions with $SmCo_5$ spin sources and a spin-exchange-relaxation-free comagnetometer, Phys. Rev. D **95**, 075014 (2017).
[42] T. W. Kornack, R. K. Ghosh, and M. V. Romalis, Nuclear spin gyroscope based on an atomic comagnetometer, Phys. Rev. Lett. **95**, 230801 (2005).
[43] Z. Xu, K. Wei, X. Heng, X. Huang, and Y. Zhai, Critical dynamics of strongly interacting ensembles in spin-exchange-relaxation-free comagnetometers, Phys. Rev. Appl. **18**, 044049 (2022).
[44] T. W. Kornack and M. V. Romalis, Dynamics of two overlapping spin ensembles interacting by spin exchange, Phys. Rev. Lett. **89**, 253002 (2002).
[45] M. Padniuk, E. Klinger, G. Łukasiewicz, D. Gavilan-Martin, T. Liu, S. Pustelny, D. F. Jackson Kimball, D. Budker, and A. Wickenbrock, Universal determination of comagnetometer response to spin couplings, Phys. Rev. Res. **6**, 013339 (2024).
[46] F. Ficek, P. Fadeev, V. V. Flambaum, D. F. Jackson Kimball, M. G. Kozlov, Y. V. Stadnik, and D. Budker, Constraints on exotic spin-dependent interactions between matter and antimatter from antiprotonic helium spectroscopy, Phys. Rev. Lett. **120**, 183002 (2018).
[47] L. Cong, F. Ficek, P. Fadeev, and D. Budker, Improved constraints on exotic interactions between electron and proton in hydrogen, arXiv:2408.11009.
[48] A. Arvanitaki and A. A. Geraci, Resonantly detecting axion-mediated forces with nuclear magnetic resonance, Phys. Rev. Lett. **113**, 161801 (2014).
[49] C. Liu, Z. Xu, K. Wei, D. Gong, X. Heng, X. Huang, W. Quan, and Y. Zhai, Modeling and suppression of atomic comagnetometer's response to micro-vibration, Sens. Actuators, A **359**, 114503 (2023).
[50] Z. Xu, K. Wei, C. Liu, X. Heng, X. Huang, D. Gong, F. Wang, Y. Zhai, and W. Quan, Analysis and suppression for critical optical non-orthogonal noise in SERF comagnetometers, IEEE Trans. Instrum. Meas. **73**, 1501709 (2024), https://xplorestaging.ieee.org/document/10494697.
[51] M. C. Tayler, T. Theis, T. F. Sjolander, J. W. Blanchard, A. Kentner, S. Pustelny, A. Pines, and D. Budker, Invited review article: Instrumentation for nuclear magnetic resonance in zero and ultralow magnetic field, Rev. Sci. Instrum. **88**, 091101 (2017).
[52] M. Jiang, J. Bian, Q. Li, Z. Wu, H. Su, M. Xu, Y. Wang, X. Wang, and X. Peng, Zero-to ultralow-field nuclear magnetic resonance and its applications, Fundam. Res. **1**, 68 (2021).
[53] M. Ledbetter, C. Crawford, A. Pines, D. Wemmer, S. Knappe, J. Kitching, and D. Budker, Optical detection of NMR J-spectra at zero magnetic field, J. Magn. Reson. **199**, 25 (2009).
[54] M. Jiang, T. Wu, J. W. Blanchard, G. Feng, X. Peng, and D. Budker, Experimental benchmarking of quantum control in zero-field nuclear magnetic resonance, Sci. Adv. **4**, eaar6327 (2018).
[55] M. Jiang, R. P. Frutos, T. Wu, J. W. Blanchard, X. Peng, and D. Budker, Magnetic gradiometer for the detection of zero-to ultralow-field nuclear magnetic resonance, Phys. Rev. Appl. **11**, 024005 (2019).
[56] Z. Xu, G. Tian, D. Gong, L. Cong, D. Budker, W. Ji, and K. Wei, Search for spin-1 new bosons by exotic spin-dependent force (to be published).

End Matter

Data processing—The angular position of the rotating spin source is indicated by the pulse in Fig. 4(a). The projection of exotic field along the sensitive axis b_y^n is approximately a sinusoidal field; see Fig. 4(b). The response of the comagnetometer to b_y^n is simulated based on measured parameters and is shown in Fig. 4(c). The corresponding experimental data from the comagnetometer are shown in Fig. 4(d). The responses to the exotic field can be divided into multiple periods based on the pulse marker and phase shift. A slight drift is observed in the experimental data, attributed to air convection disturbances and temperature fluctuations.

As shown in Fig. 4(d), the data are divided into segments, with each segment corresponding to one modulation period. Using linear interpolation between consecutive pulses, each segment is further divided into two parts, corresponding to two half-periods. Then the mean value of each segment is derived and denoted as $\bar{S}_i^+$ and $\bar{S}_i^-$ for the positive and negative parts, respectively. Assuming that the background signal is time dependent, we can use the

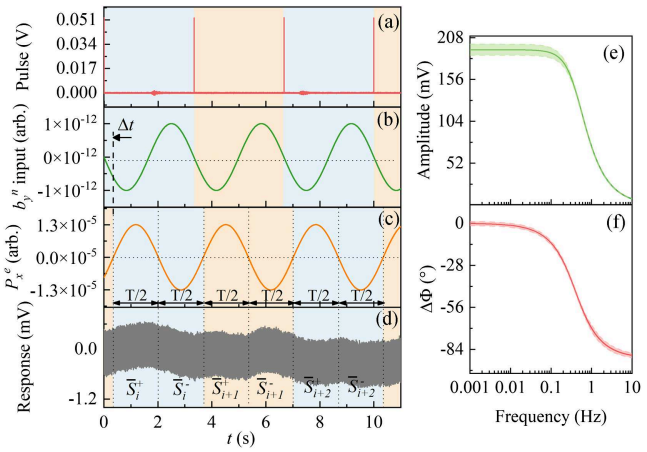

FIG. 4. Data acquisition process. (a) The motor decoder generates one pulse per revolution. (b) As the motor rotates, the projection of the exotic field b_y^n on the y axis produces an effective sinusoidal magnetic field. (c) The simulated response of the comagnetometer shift is phase relative to the input. (d) The measured response of the comagnetometer. The simulated (e) amplitude and (f) phase response of the comagnetometer to b_y^n in the self-compensation regime. The uncertainty bands are calculated based on the uncertainties of the measured parameters in the text.

following procedure to remove the dc bias field and low-frequency drifts and get the effective amplitude of the signal for the i th period of the data [25]:

$$\bar{S}_i = \frac{1}{8}[\bar{S}_i^+ - 3\bar{S}_i^- + 3\bar{S}_{i+1}^+ - \bar{S}_{i+1}^-]. \tag{A1}$$

We further consider the phase shift between the sensor response S and the exotic field b_y^n. In Fig. 4(f), the phase shift is calculated based on the measured parameters $R_2^n = 0.030(2)\,\mathrm{rad/s}$, $R_2^e = 5430(200)\,\mathrm{rad/s}$, $P_z^e = 0.75(11)$, $B_c = 506(1)\,\mathrm{nT}$, $B_z^n = 407(7)\,\mathrm{nT}$, and $B_z^e = 100(7)\,\mathrm{nT}$ [25]. The shaded area of the curve is the corresponding uncertainty. The phase shift is $\Delta\Phi = -36.3(16)°$ at modulation frequency 0.3 Hz [corresponding to a time delay of $\Delta t = 0.33(2)$ s]. The signal segments shown in Figs. 4(c) and 4(d) are shifted correspondingly by Δt. The comagnetometer has similar response forms to the exotic field b_y^n and the usual magnetic field B_y, which is $S = K_{b_y^n} b_y^n + K_{B_y} B_y$, where $K_{b_y^n}$ and K_{B_y} are the respective scale factors. Hence, the exotic field b_y^n can be calibrated using a usual magnetic field, which is a common method in experiments searching for new physics beyond the standard model [25,42,45]. We first determine the scale factor of the dc exotic field b_y^n, $K_{b_y^n}^{\mathrm{dc}}$, using the response to the usual magnetic field. Then we obtain the $K_{b_y^n}^{\mathrm{ac}}$ with the ratio $K_{b_y^n}^{\mathrm{ac}}/K_{b_y^n}^{\mathrm{dc}}$ from Fig. 4(e). For 0.3 Hz ac signal, $K_{b_y^n}^{\mathrm{ac}}$ is determined to be 0.84(6). The error of the calibration factor is obtained from long-term monitoring with the error transmission in Ref. [25].